Research Article | Vol. 31, No. 7 / 27 Mar 2023 / Optics Express 11227
Optics EXPRESS

Thermal metasurface with tunable narrowband absorption from a hybrid graphene/silicon photonic crystal resonance

ARUN NAGPAL,[1] MING ZHOU,[2] OGNJEN ILIC,[3] ZONGFU YU,[4] AND HARRY A. ATWATER[1,*]

[1]Thomas J. Watson Laboratory of Applied Physics, California Institute of Technology, 1200 E. California Avenue, Pasadena, CA 91125, USA
[2]Department of Electrical Engineering, Stanford University, 450 Serra Mall, Stanford, CA 94305, USA
[3]Department of Mechanical Engineering, University of Minnesota, 111 Church Street SE, Minneapolis, MN 55455, USA
[4]Department of Electrical and Computer Engineering, University of Wisconsin, 1415 Engineering Drive, Madison, WI 53706, USA
*haa@caltech.edu

Abstract: We report the design of a tunable, narrowband, thermal metasurface that employs a hybrid resonance generated by coupling a tunable permittivity graphene ribbon to a silicon photonic crystal. The gated graphene ribbon array, proximitized to a high quality factor Si photonic crystal supporting a guided mode resonance, exhibits tunable narrowband absorbance lineshapes ($Q > 10{,}000$). Actively tuned Fermi level modulation in graphene with applied gate voltage between high absorptivity and low absorptivity states gives rise to absorbance on/off ratios exceeding 60. We employ coupled-mode theory as a computationally efficient approach to elements of the metasurface design, demonstrating an orders of magnitude speedup over typical finite element computational methods.

1. Introduction

Over the past decade, graphene has been the subject of intensive research on extreme light confinement at mid-infrared wavelengths [1,2] and has emerged as a versatile element for tuning the complex refractive index in optical devices operating in this wavelength range [3,4]. An attractive feature of graphene is the observation of tunable, confined plasmons, particularly in patterned materials, where a large plasmonic wavevector relative to free space values enables confinement at feature sizes well below the operating free space wavelength [5–7]. Graphene localized surface plasmon resonances (LSPR) are tunable by Fermi level modulation via application of a gate voltage, modulating the graphene carrier density and changing the plasmonic permittivity and coupling strength to its environment. This mechanism has stimulated efforts to realize dynamic metasurfaces that employ graphene as an electrically tunable element, in applications including spatial light modulation [8,9], electrical switching [10], and chemical fingerprinting [11,12]. Metasurfaces that actively control radiation from thermal emitters have potential to enable advances in infrared applications, including chemical fingerprinting, thermal imaging, and infrared energy harvesting.

Recently, much interest has been paid in the development of nanophotonic thermal metasurface designs to enable desired emissivity and absorptivity characteristics [13–17]. While the complex permittivity of graphene can readily vary by gated Fermi level modulation, graphene exhibits a low intrinsic absorptivity of ~2.3% at infrared and optical frequencies. Considerable effort has thus been devoted resonant enhancement of absorption in graphene and approaches to realize absorptance values much greater than the intrinsic value have been reported [18–22]. Realizing perfect (unity) absorption in graphene is challenged by degradation of carrier mobilities

#470198 https://doi.org/10.1364/OE.470198
Journal © 2023 Received 20 Jul 2022; revised 28 Sep 2022; accepted 30 Sep 2022; published 20 Mar 2023

Optics EXPRESS

resulting from graphene nanofabrication processes. While mobilities in excess of 100,000 cm^2/(V s) [23] are achievable in pristine monolayer graphene, mobilities below 2000 cm^2/(V s) are typical in nanoscale ribbons [24] due to polymer residues [25] or trapped adsorbates [26]. To overcome this challenge, electromagnetic design of nanostructures for critical coupling of graphene monolayers to free space have demonstrated near-unity peak absorptivity values [27–32]. In such configurations, radiation from the absorbing layer destructively interferes with reflected light at the topmost interface of a reflectarray metasurface. As is typical with plasmonics, metasurfaces based on graphene LSPRs suffer from low quality factor relative to dielectric-based varieties. As such, graphene-based devices would benefit from the incorporation of additional, non-absorbing resonant elements, that produce more tailored resultant absorption characteristics, such as higher quality factor resonances. Such approaches, incorporating bound states in the continuum [33], or split ring resonators [34], have resulted in devices exhibiting Q-factors on the order of thousands. However, the physical analysis of such coupled structures is complex, due to the presence of multiple interacting photonic modes in the regime of critical coupling. To overcome the computational cost required to understand the behavior of such devices, temporal coupled-mode theory (CMT) has been successfully used to model the scattering parameters of devices consisting of such interacting resonant elements [35].

Here, we theoretically report a coupled mode metasurface that consists of a graphene ribbon array coupled to a 1-D photonic crystal supporting a guided mode. We note that structures involving critically coupling graphene plasmons to 1-D photonic crystals have been investigated under a variety of conditions in literature [36–45]. Our result distinguishes itself from previous works through analysis of the coupled-mode nature of the resultant metasurface. Previously, such coupled metasurfaces would be designed by extensive, computationally costly parameter sweeping of geometry and wavelength. Using temporal coupled-mode theory, we analyze the hybrid response of the metasurface via the isolated resonant elements. The optimization of isolated guided mode and localized surface plasmon resonances is much less computationally expensive and offers predictive power for the center wavelength and linewidth of the resultant absorptance characteristic. Furthermore, the shared discrete symmetry of the graphene ribbon array and the photonic crystal design results in a device that is easily scalable to other wavelengths in the MIR through simple and well-known geometric scaling relations. Finally, a realistic graphene mobility is considered, and we show that the coupled mode theory analysis retains predictive capability for realistic graphene material constants. The metasurface supports a critically coupled spectrally narrowband absorptance lineshape with an exceptionally high-Q of greater than 10,000. Remarkably, our metasurface is tunable from a near-unity absorptance 'on' state and a near-background absorptance 'off' state as we sweep the graphene Fermi level from 500meV to 100meV.

2. Device structure

A unit cell of our hybrid graphene/silicon photonic crystal structure incorporates two resonant modes: a lossy plasmonic mode originating from the LSPR of a graphene ribbon array, and the nearly lossless guided-mode resonance (GMR) of a one-dimensional silicon photonic crystal zero contrast grating structure. The graphene ribbons can be gated, providing control over the graphene complex conductivity and thus the center wavelength and width of the LSPR via tuning the Fermi level. Shown in Fig. 1(a) are finite element electromagnetic simulations of 55 nm graphene ribbons encapsulated in a medium with n = 1.3693, approximating the index of CaF_2 at 7 μm. The FEM simulations utilize a model of graphene conductivity, calculated analytically from [46], which is parameterized by wavelength, Fermi energy, temperature, and scattering rate. We choose a realistic graphene scattering energy of 350 meV, accounting in part for carrier density-dependent scattering and for disorder induced through etching the graphene into ribbons. The assumed carrier mobility of 1180 cm^2/(V-s) is sufficiently low to be realized experimentally.

Optics EXPRESS

The resultant ribbon characteristics agree with previously reported experimental measurements [47]. Designs incorporating un-patterned graphene result in lower quality factor modes for a given operating wavelength and are subject more strongly to fluctuations in mobility for higher Fermi levels. Furthermore, ribbons can be individually addressed, for applications in MIR spatial light modulation and imaging, in contrast to many previously reported devices that utilize single layers of graphene. The photonic crystal consists of a slab index-matched to a grating. The reflectance of the photonic crystal exhibits the characteristics of a high-Q narrowband bandpass filter, as shown in Fig. 1(d).

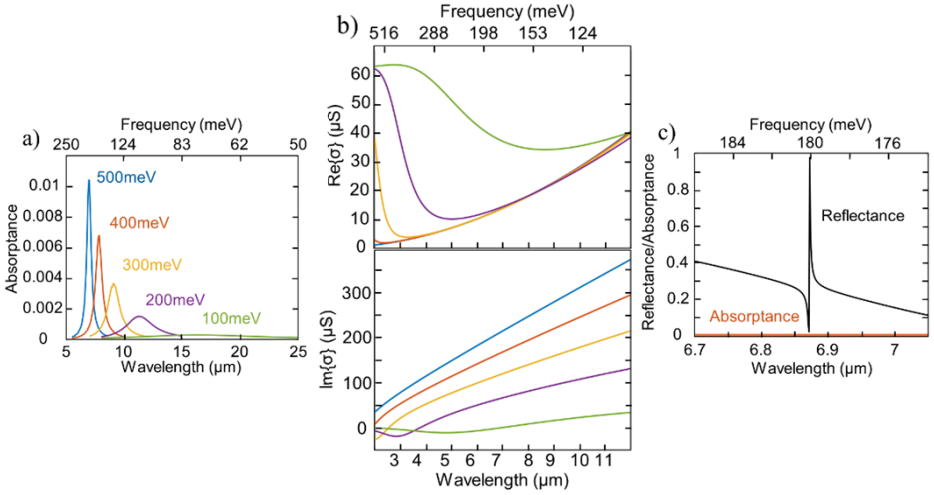

Fig. 1. (a) FEM simulations of the LSPR resonances of 55 nm graphene ribbons encapsulated in lossless CaF_2 (n = 1.3693), as a function of Fermi level. (b) The real (top) and imaginary (bottom) parts of graphene conductivity, calculated with the random phase approximation (RPA), at 300 K. The calculation was made using analytic expressions from [46]. The scattering rate was chosen to be 350 meV. The colored labels in Fig. 1(a) correspond to the colored traces in Fig. 1(b) as well. (c) The reflectance (black trace) and absorbance (red trace) spectra of the guided mode resonance structure. The index is chosen to be approximately equal to a-Si at 7 μm, n = 3.42. The Q factor is approximately 3,312.

We choose the height of the slab waveguide portion of the photonic crystal to be equal to one-half of the unit cell period, and the grating height is taken to be small with respect to the other dimensions, thus producing a weakly modulated waveguide mode index, which supports a high-quality resonance through the interference of a leaky slab waveguide mode with a confined grating one [48]. A schematic of the unit cell of our hybrid resonator is shown in Fig. 2(a). The metasurface is characterized by several geometrical parameters: N_h = grating height, S_h = slab waveguide thickness, g_d = top dielectric spacer layer thickness, b_d = bottom dielectric spacer layer thickness, Λ = unit cell period, f = fill factor, w_g = graphene ribbon width, and n_i = refractive index of layer i. The device is in a reflectarray configuration, with a thick backreflector, depicted as the yellow layer in Fig. 2(a), as the bottom layer above the substrate. The calculations forthcoming take this layer to be a perfect electric conductor, however, assuming standard material constants for evaporated gold does not substantially change the device geometry or performance for MIR wavelengths. For all resonators investigated here, the fill factor f was chosen to be 0.5, $n_0 = 1$, and $n_1 = 3.42$, corresponding to the refractive index of amorphous silicon at 7 μm. As the Fermi level changes from 500meV to 100meV, the graphene LSPR transitions out of resonance with the photonic crystal, modifying the coupling strength between the two modes. We note that the periodicity of the graphene array is set by the photonic crystal period and is an order of

Optics EXPRESS

magnitude larger than the width of ribbons themselves. Thus, we expect no near-field plasmonic mode coupling between adjacent graphene ribbons. The result is a hybrid resonator response that can be modulated electrically, through electrostatically gating the graphene ribbons. The absorptance characteristic of the metasurface as a function of Fermi level is shown in Fig. 2(b). The near unity absorptance state occurring at a ribbon Fermi level of 500 meV can be termed an 'on' state, where the absorptivity (and by Kirchhoff's Law, the emissivity) is maximized at the operating wavelength of 7.02 μm. As graphene ribbon LSPRs only support transverse-magnetic (TM) polarized excitations, and the GMR is strongly angle- and polarization-dependent, unless indicated otherwise, all calculations assume normal incidence with TM polarization.

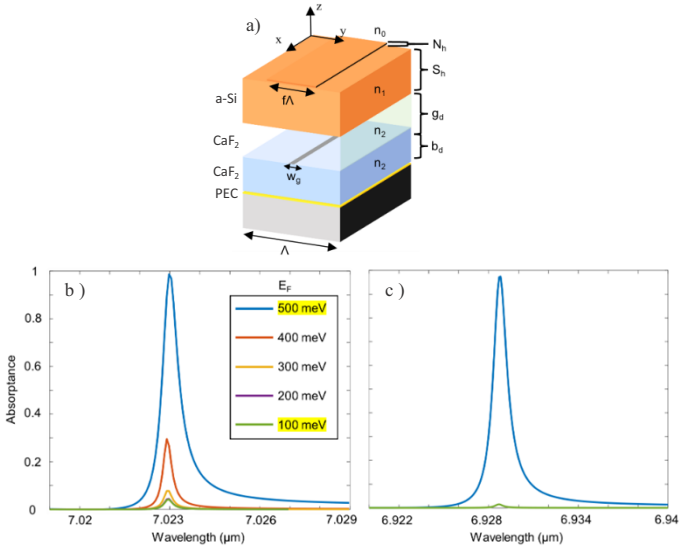

Fig. 2. (a) A schematic of the metasurface unit cell. Periodic boundary conditions are applied along the y-axis and the x-axis is presumed to be infinitely continuous. (b) The absorptance characteristic of the unit cell demonstrating high quality factor as a function of Fermi level for the following parameters: $N_h = 20$ nm, $S_h = 2.095$μm, $g_d = 1.375$μm, $b_d = 687.5$ nm, $\Lambda = 4.19$μm, $w_g = 55$ nm, $n_2 = 1.3693$. The Q-factor is approximately 10,328, and the on/off ratio is 23.6. In this case, the on/off ratio is the ratio of absorbance maxima at 500 meV to 100 meV. The graphene conductivity model employed here is shown in Fig. 1(b),(c) assuming an ambient temperature of 300 K. The 'on' and 'off' state Fermi levels are highlighted in the legend. (c) The absorptance characteristic of the unit cell demonstrating high on/off ratios as a function of Fermi level for the following parameters: $N_h = 20$ nm, $S_h = 2.125$μm, $g_d = 1.718$μm, $b_d = 3.436$μm, $\Lambda = 4.25$μm, $w_g = 103$ nm, $n_2 = 1.12$. The Q-factor is approximately 6,103, and the on/off ratio is 64.93. The graphene conductivity model employed here assumed an ambient temperature of 20 K. The trace colors correspond to the legend shown in (b) – the 'on' state at 500 meV in blue, and the 'off' state at 100 meV in green.

Conversely, the absorptance characteristic that results at a Fermi level of 100 meV is a minimum in absorptance, where the response at the operating wavelength is nearly indistinguishable from the background, can be termed the 'off' state. A pertinent metric for the performance of this hybrid resonator is the absorptance ratio between the "on" and the "off" states, at the operating wavelength. Shown in Fig. 2(b) and (c) are two resonator geometries that vary this on/off ratio at the expense of quality factor. Note that despite relatively modest graphene ribbon absorptance maxima depicted in Fig. 1(a), the resultant absorptance characteristics shown in Fig. 2 are near unity, demonstrating almost perfect absorptance. This is due to the tuning of the cavity distance

Optics EXPRESS

around the ribbon array, such that the graphene is critically coupled to the GMR within the photonic crystal.

A consequence of the discrete periodicity shared by the graphene ribbon arrays and the photonic crystal grating is a strongly anisotropic transverse-electric (TE) versus transverse-magnetic (TM) device response. Figure 3 breaks down the difference in the TM and TE characteristics for the isolated resonances and the thermal metasurface designed in Fig. 2(b). In Fig. 3(a), the dipole and quadrupole responses of the graphene ribbon LSPR are identified at 7 μm and 5 μm respectively. As expected, the LSPR only appears under TM polarization due to the TM-polarized plasmons. The photonic crystal on the other hand, due to the isotropy of the underlying Fabry-Perot mode, exhibits similar background reflectance characteristics with the sharp GMR resonances depending on polarization, as shown in Fig. 3(b). Due to the proximity of the dipole and quadrupole resonances to separate GMRs in the photonic crystal, shown in the boxed portions of the spectrum in Fig. 3(b), the MIR absorptance characteristic of the thermal metasurface has two peaks under TM illumination – the critically-coupled response at 7 μm and an additional peak near the ribbon quadrupole response. This can be seen in Fig. 3(c). As is the case with the ribbon array, the response is greatly suppressed under TE compared to TM. Furthermore, since the TE and TM directions are decoupled from one another, the device could be made polarization insensitive simply by imposing periodicity in orthogonal in-plane directions.

The consequences of the anisotropy between the TM and TE device response are especially apparent when considering the operation of the metasurface as an emitter. By Kirchhoff's Law, the emission and absorption at a given angle and wavelength are reciprocal. Thus, by designing a suppressed TE absorption spectrum, we expect that, upon heating, this device will emit almost entirely narrowband TM polarized radiation. Thus, coupled-mode devices are promising for controlling otherwise spontaneous degrees of freedom of thermal emission.

Critical coupling of an absorber to a resonant cavity requires precise tuning of the device geometry required to achieve decay rate matching [30–31]. Using full-wave simulations, this requires substantial computational power, through the running of many simulations. One method to simplify this process involves using computationally efficient approaches to approximate the response of the metasurface, requiring many fewer computationally expensive full-wave simulations. Temporal coupled-mode theory accurately reproduces the response of the metasurface over a range of geometries. To apply the theory, we consider the photonic crystal and ribbon array as homogeneous slabs and use a plane wave to model the incident field. Each resonator is modelled using the matrix equation

$$\mathbf{S}(\omega) = \mathbf{C} + \frac{\mathbf{d}_i \mathbf{d}_i^T}{i(\omega - \omega_0) + \gamma} \tag{1}$$

Here, $\mathbf{S}$ and $\mathbf{C}$ are scattering matrices, where $\mathbf{C}$ is the direct scattering process of a homogenous slab, and ω, ω_0, and γ are the frequency, mode resonant frequency, and mode radiative decay rate respectively. These and the vector of coupling coefficients to all output channels $\mathbf{d}$ are fitted phenomenologically from individual FEM simulations of the isolated resonators, shown diagrammatically in Fig. 4(a). The rank of the matrices given above is determined by the number of input and output ports for the device, illustrated in Fig. 4(a). The graphene resonance fitting illustrates another advantage of our design: the strong oscillator strengths of graphene ribbons result in well-defined resonances that can be fit using this theory, in contrast to the much lower Q factor sheet plasmons in un-patterned monolayers. With respect to the graphene ribbons, analytical expressions for the coupling rates and direct scattering process have been determined in the coupled-mode formalism based on the symmetry of the monolayer and the relative transparency

Optics EXPRESS

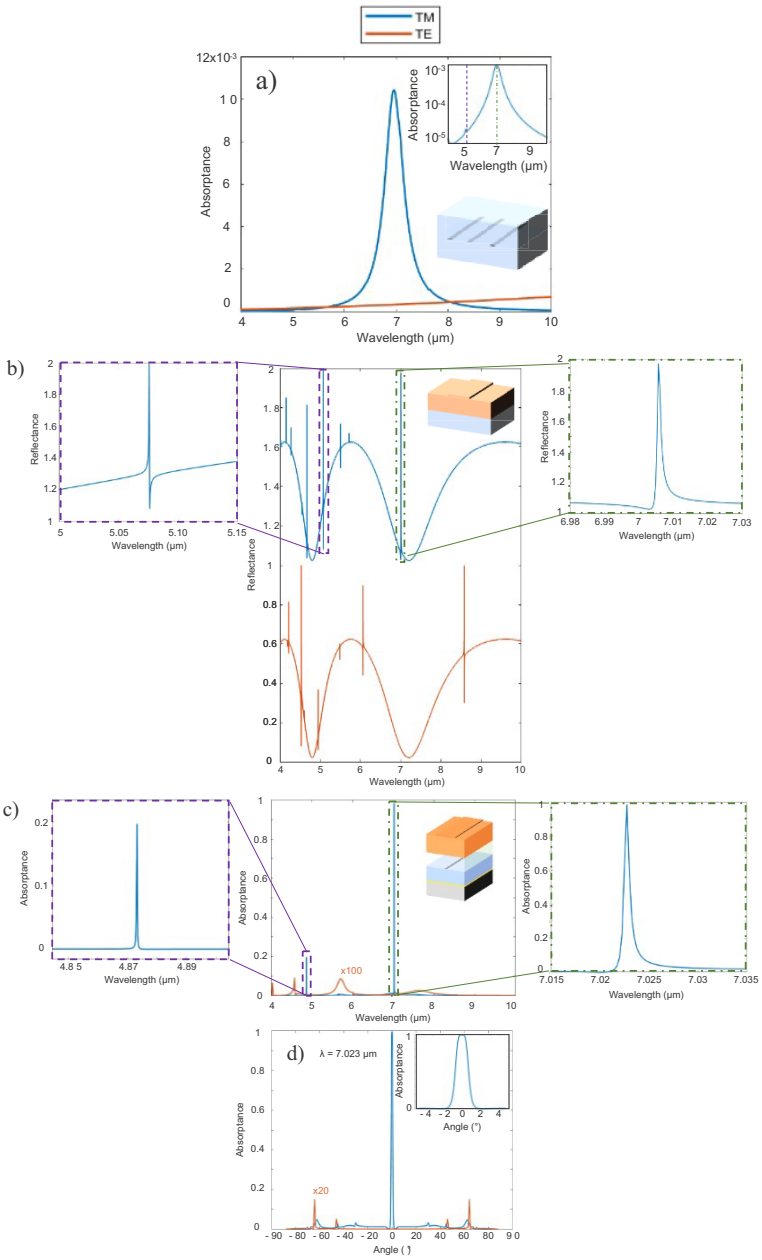

Fig. 3. (a) Absorptance characteristics of graphene nanoribbon array encapsulated in an n = 1.3693 medium under TE and TM polarization at normal incidence. Inset: Log-linear plot of absorptance under TM polarization, with the quadrupole at 5 μm and the dipole at 7 μm indicated by the purple dashed and green dot-dashed lines respectively. (b) Photonic crystal reflectance characteristic under TM and TE polarization at normal incidence. TM and TE curves are offset for clarity. (c) The coupled thermal metasurface absorptance under normal incidence for TE and TM polarizations. The TE response is multiplied by a factor of 100 for visibility. The purple dashed and green dot-dashed boxes in (b) and (c) are zoomed in portions of the given spectra near the graphene quadrupole and dipole resonances respectively. (d) Absorptance as a function of incidence/emission angle for the thermal metasurface for TM and TE polarizations. TE polarization is multiplied by a factor of 20 for visibility. Inset: TM-illuminated absorptance characteristic near normal incidence. For all plots, the TM mode is drawn using a blue trace and the TE mode is drawn using an orange trace.

Optics EXPRESS

of the material outside of the resonant plasmonic response. For the graphene nanoribbons:

$$\mathbf{C}_{GR} = \begin{pmatrix} 0 & 1 \\ 1 & 0 \end{pmatrix} \tag{2}$$

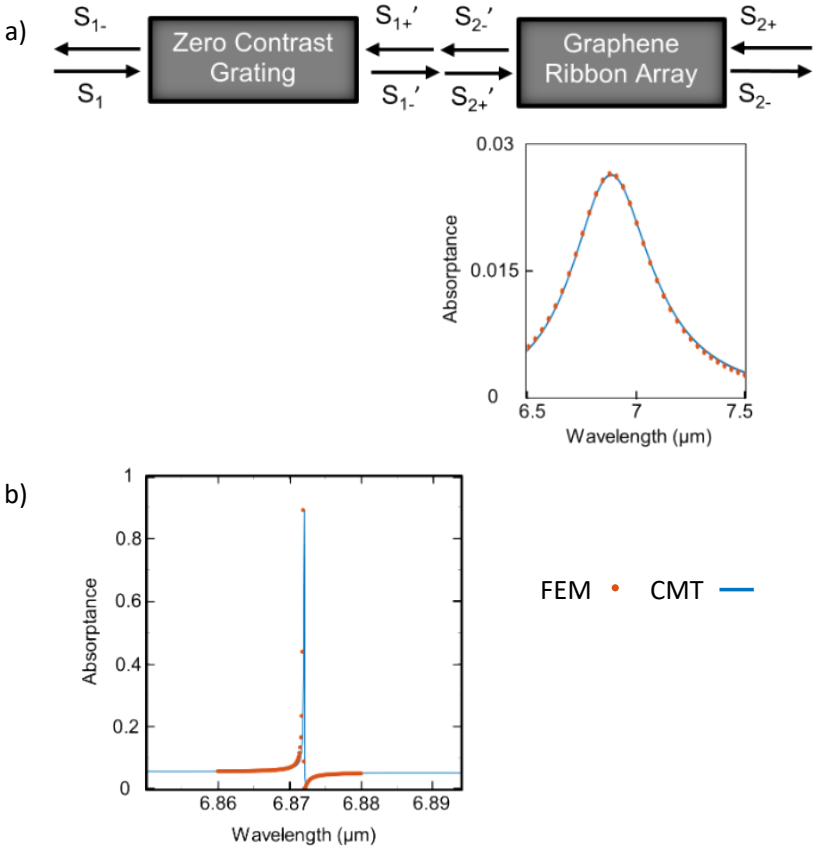

Fig. 4. (a) A diagram of the CMT calculation, with a-priori FEM simulations of each of the resonant devices individually, phenomenologically fit using the formalism from [35]. (b) An example of a resultant absorption spectrum fitted using CMT, indicating good agreement. The device parameters in this case are: $N_h = 20$ nm, $S_h = 2.125$μm, $g_d = 14.8$μm, $b_d = 2$μm, $\Lambda = 4.25$μm, $w_g = 100$ nm, $n_0 = n_2 = 1$.

$$\mathbf{d}^{GR} = i\sqrt{\frac{\gamma_r^{GR}}{2}} \begin{pmatrix} 1 \\ 1 \end{pmatrix} \tag{3}$$

where γ_r^{GR} is the radiative decay rate of the graphene ribbon array. Since the graphene has intrinsic loss, to accurately model the scattering matrix of the array, we must include one free parameter which we choose to be the ratio of the radiative to intrinsic decay. Note that the coupling rate in and out of the i^{th} port is related to the vector $\mathbf{d}$ by:

$$d_i^* d_i = \frac{2}{\tau_i} \tag{4}$$

In the case of the photonic crystal, the resonator can be approximated as a flat slab with the strongly coupled guided modes superimposed. In this approximation, the resonator is treated as

Optics EXPRESS

a homogenous slab, with optical thickness l taken to be a free parameter. Since we chose the grating to be thin with respect to the thickness of the index-matched slab, and because we are taking the material to be lossless, the value should be close to the real thickness of the photonic crystal slab. This is illustrated in Fig. 5 – the Fabry-Perot characteristic of a silicon slab atop a half space of CaF_2 agrees closely, though not perfectly, to the slowly varying part of the photonic crystal reflectance characteristic.

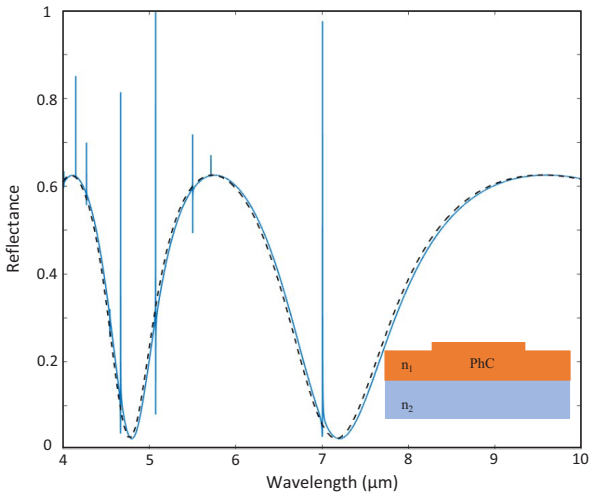

Fig. 5. The reflectance characteristic (solid line) of the photonic crystal at normal incidence for TM polarization, described in Fig. 2, compared to the Fabry-Perot characteristic of a slab on an infinite CaF_2 substrate (dashed line).

Thus, the direct scattering matrix simply applies the reflection and transmission Fresnel coefficients for our constructed slab with thickness l:

$$\mathbf{C}_{PhC} = \begin{pmatrix} r & t \\ t & r \end{pmatrix} \tag{5}$$

However, the decay rates and coupling coefficients **d** for the input and output channels can be related to each other and are governed by the asymmetry of the structure [49].

$$(d_2^{PhC})^* = -\frac{1}{t}[d_1^{PhC} + r(d_1^{PhC})^*] \tag{6}$$

$$\frac{\tau_1}{\tau_2} = 1 + 2\left(\frac{r}{t}\right)^2 + 2\left(\frac{r}{t^2}\right)\cos\phi \tag{7}$$

where r and t are the Fresnel coefficients for the slab and ϕ is the relative phase between the input and output coupling coefficients, taken as a third free parameter. This parameter corresponds to the additional phase contributed to impinging plane waves by the guided mode in the photonic crystal, and effects the phenomenological fit to the photonic crystal shown in Fig. 4(a).

An essential, though computationally expensive part of designing critically coupled systems originates from the determination and tuning of the geometric parameters that most influence critical coupling. In this case, one of the advantages of a design approach incorporating coupled-mode analysis is that most of the device parameters are set a-priori to determine the desired individual resonator characteristics discussed previously. The only parameters that are relevant to the critical coupling condition in this device are then the dielectric layer thicknesses, g_d and

Optics EXPRESS

b_d. Thus, once the relevant parameters in Eq. (1) are chosen or computed, the S-matrix for each individual resonator can be found and a transfer matrix expression for the entire device can be computed. Since few-element transfer matrix calculations are much faster than FEM simulations, many spectra can be computed for many different values of g_d and b_d, making searches for the critical coupling condition much less computationally expensive. Figure 6 depicts the application of CMT to determine the values of g_d and b_d that result in near-unity absorptance.

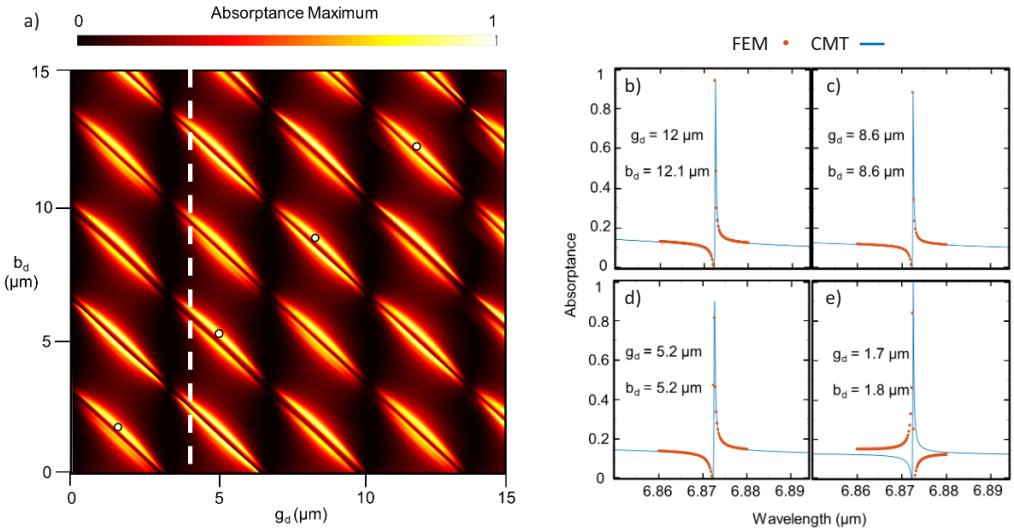

Fig. 6. (a) The phase space of g_d and b_d (dielectric spacer layer thicknesses) as computed by CMT. We note the ~λ/4 periodicity results from the Fabry-Perot character of the total dielectric cavity, and the constructive interference condition for critical coupling. The dashed line indicates a value of approximately 1 unit cell period. The white dots indicate the coordinates for the traces on the right. (b)-(d) Located at coordinates (12 μm, 12.1 μm), (8.6 μm, 8.6 μm), and (5.2 μm, 5.2 μm) respectively. The CMT result matches closely to the FEM calculation. These configurations are on the right-hand side of the phase space, indicating a separation between the GMR structure and the ribbon array of more than 1 wavelength. (e) Located at coordinates (1.7 μm, 1.8 μm), CMT calculation proves to be a poor fit to the FEM simulation.

We also note that the matching discrete translational symmetry of each of the coupled resonant elements are advantageous from a design standpoint due to LSPRs being trivially scalable over the entire MIR range. The devices shown here operate at 7 μm, but since it is well-known that LSPR resonant wavelength $\lambda_{0,GR}$ scales with ribbon width W like $\lambda_{0,GR} \sim W^{-0.5}$, and the GMR resonant wavelength $\lambda_{0,PhC}$ scales with photonic crystal period Λ like $\lambda_{0,PhC} \sim \Lambda$, one could adapt this design to create emitters operating anywhere over the mid- to far- infrared. Material dispersion would modify the critical coupling condition at other wavelengths, however the use of CMT to calculate the perfect absorption condition reduces the computational cost and time of designing the device substantially, as only g_d and b_d would have to be recomputed.

However, since our CMT calculation assumes translational symmetry in the x-y plane, it correctly predicts the response only for devices of sufficient size – this corresponds to points to the right of the dashed line in Fig. 6(a). When the region around the graphene ribbon is within the near-field of the GMR structure, the plane-wave approximation breaks down and the transfer matrix formalism fails to produce the correct lineshape. Figure 5(e) exemplifies such a point where near-field coupling impacts the accuracy of the results. The lineshape predicted by CMT is inverted compared to the profile obtained via full-wave simulation. Figure 7 illustrates this

Optics EXPRESS

near-field coupling directly: in Figs. 7(a) and (b), it can be seen the field vectors around the GMR structure lose their plane wave character for a distance of approximately 1 metasurface lattice period beyond the structure, after which the plane wave character is recovered.

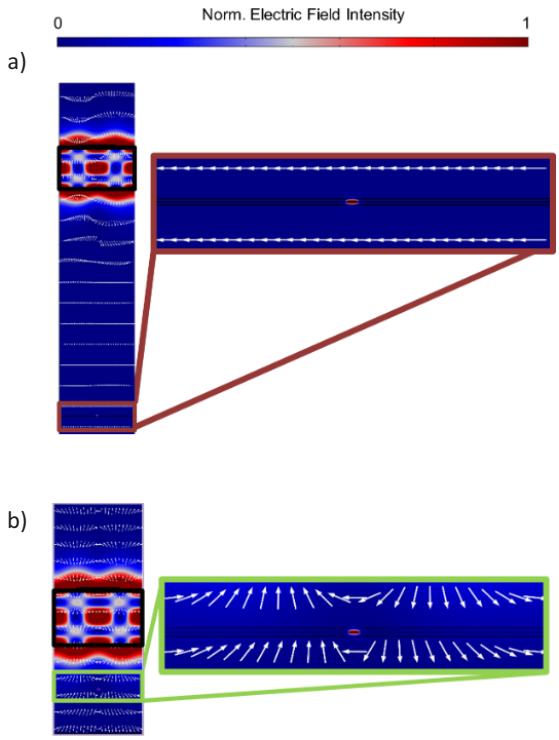

Fig. 7. (a) The electric field intensity profile for the device modeled in Fig. 5(b). The area around the graphene ribbon is expanded in the maroon box, with the graphene ribbon LSPR field shown. (b) The electric field intensity profile for the device modelled in Fig. 5(e). The region around the graphene ribbon is expanded in the green box. The white arrows are the total electric field vectors at a point. The photonic crystal is indicated with thick black lines.

Another remarkable property of these emitters demonstrated in Fig. 7 is that the total source of emission consists of an extremely small fraction of the cross-section of the emitter. In the devices shown here, the graphene ribbon array, magnified and depicted to the right of the device cross-section, consists of 1.3% of the total area of the array. This is indicative of the remarkable efficiency with which the critically coupled devices channel incoming radiation into the lossy element.

3. Conclusion

In summary, we have proposed the design for a thermal metasurface with a tunable ultra-narrow absorptance lineshape through coupling of a high-Q lossless GMR in a dielectric photonic crystal with the LSPRs of a graphene ribbon array. The hybrid resonator exhibits a Q factor exceeding 10,000. We also showed that this resonance can be tuned electrostatically from a near-unity condition to one nearly indistinguishable from thermal background, with an on/off ratio greater than 60. We can recover the lineshape to high accuracy by fitting resonance parameters of the GMR and LSPR using coupled mode theory, which was used to predict the critical coupling conditions as a function of metasurface geometrical parameters. Such hybrid graphene silicon

Optics EXPRESS

photonic crystal resonators are promising elements to enable design of complex active thermal metasurfaces for mid-to-far infrared optical modulation applications.

Funding. Defense Advanced Research Projects Agency (HR00111820046).

Acknowledgments. The authors thank Michelle Povinelli and Shanhui Fan for useful discussions.

Disclosures. The authors declare no conflicts of interest.

Data availability. Data underlying the results presented in this paper are available from the corresponding authors upon reasonable request.

References

1. I. Epstein, D. Alaraz, Z. Huang, V.-V. Pusapati, J.-P. Hugonin, A. Kumar, X. M. Deputy, T. Khodkov, T. G. Rappoport, J.-H. Hong, N. M. R. Peres, J. Kong, D. R. Smith, and F. H. L. Koppens, "Far-field excitation of single graphene plasmon cavities with ultracompressed mode volumes," Science **368**(6496), 1219–1223 (2020).
2. V. Brar, M. S. Jang, M. Sherrott, J. J. Lopez, and H. A. Atwater, "Highly confined tunable mid-infrared plasmonics in graphene nanoresonators," Nano Lett. **13**(6), 2541–2547 (2013).
3. J. Brouillet, G. T. Papadakis, and H. A. Atwater, "Experimental demonstration of tunable graphene-polaritonic hyperbolic metamaterial," Opt. Express **27**(21), 30225–30232 (2019).
4. L. Ju, B. Geng, J. Horng, C. Girit, M. Martin, Z. Hao, H. A. Bechtel, X. Liang, A. Zettl, Y. R. Shen, and F. Wang, "Graphene plasmonics for tunable terahertz metamaterials," Nat. Nanotechnol. **6**(10), 630–634 (2011).
5. M. Jablan, H. Buljan, and M. Soljačić, "Plasmonics in graphene at infrared frequencies," Phys. Rev. B: Condens. Matter Mater. Phys. **80**(24), 245435 (2009).
6. F. J. García de Abajo and G. de Abajo, "Graphene plasmonics: Challenges and opportunities," ACS Photonics **1**(3), 135–152 (2014).
7. T. Low and P. Avouris, "Graphene plasmonics for terahertz to mid-infrared applications," ACS Nano **8**(2), 1086–1101 (2014).
8. B. Zeng, Z. Huang, A. Singh, Y. Yao, A. K. Azad, A. D. Mohite, A. J. Taylor, D. R. Smith, and H.-T. Chen, "Hybrid graphene metasurfaces for high-speed infrared light modulation and single-pixel imaging," Light: Sci. Appl. **7**(1), 51 (2018).
9. M. C. Sherrott, P. W. C. Hon, K. T. Fountaine, J. C. Garcia, S. M. Ponti, V. W. Brar, L. A. Sweatlock, and H. A. Atwater, "Experimental demonstration of >230° phase modulation in gate-tunable graphene-gold reconfigurable mid-infrared metasurfaces," Nano Lett. **17**(5), 3027–3034 (2017).
10. O. Kovalchuk, S. Uddin, S. Lee, and Y.-W. Song, "Graphene capacitor-based electrical switching of mode-locking in all-fiberized femtosecond lasers," ACS Appl. Mater. Interfaces **12**(48), 54005–54011 (2020).
11. N. J. Bareza, K. K. Gopalan, R. Alani, B. Paulillo, and V. Pruneri, "Mid-infrared gas sensing using graphene plasmons tuned by reversible chemical doping," ACS Photonics **7**(4), 879–884 (2020).
12. Y. Hu, ÁI López-Lorente, and B. Mizaikoff, "Graphene-based surface enhanced vibrational spectroscopy: Recent developments, challenges, and applications," ACS Photonics **6**(9), 2182–2197 (2019).
13. J. Park, J.-H. Kang, X. Liu, S. J. Maddox, K. Tang, P. C. McIntyre, S. R. Bank, and M. L. Brongersma, "Dynamic thermal emission control with InAs-based plasmonic metasurfaces," Sci. Adv. **4**, 3163 (2018).
14. T. Inoue, M. De Zoysa, T. Asano, and S. Noda, "Realization of narrowband thermal emission with optical nanostructures," Optica **2**(1), 27–35 (2015).
15. S. Vassant, I. M. Doyen, F. Marquier, F. Pardo, U. Gennser, A. Cavanna, J. L. Pelouard, and J. J. Greffet, "Electrical modulation of emissivity," Appl. Phys. Lett. **102**(8), 081125 (2013).
16. J.-J. Greffet, R. Carminati, K. Joulain, J.-P. Mulet, S. Mainguy, and Y. Chen, "Coherent emission of light by thermal sources," Nature **416**(6876), 61–64 (2002).
17. A. C. Overvig, S. A. Mann, and A. Alù, "Thermal metasurfaces: Complete emission control by combining local and nonlocal light-matter interactions," Phys. Rev. X **11**(2), 021050 (2021).
18. S. Thongrattanasiri, F. H. L. Koppens, F. J. García de Abajo, and G. de Abajo, "Complete optical absorption in periodically patterned graphene," Phys. Rev. Lett. **108**(4), 047401 (2012).
19. A. Nematpour, N. Lisi, A. Piegari, L. Lancellotti, G. Hu, and M. L. Grilli, "Experimental near infrared absorption enhancement of graphene layers in an optical resonant cavity," Nanotechnology **30**(44), 445201 (2019).
20. S. Kim, M. S. Jang, V. W. Brar, K. W. Mauser, L. Kim, and H. A. Atwater, "Electronically tunable perfect absorption in graphene," Nano Lett. **18**(2), 971–979 (2018).
21. Z. Fang, Y. Wang, A. E. Schlather, Z. Liu, P. M. Ajayan, F. J. García de Abajo, P. Nordlander, X. Zhu, and N. J. Halas, "Active tunable absorption enhancement with graphene nanodisk arrays," Nano Lett. **14**(1), 299–304 (2014).
22. Y. Yu, J. Zhou, Q. Cai, Z. Chu, J. Deng, W. Lu, Z. Li, and X. Chen, "Dynamically tunable ultra-narrowband perfect absorbers for the visible-to-infrared range based on a microgravity integrated graphene pair," Opt. Lett. **46**(9), 2236–2239 (2021).
23. K. I. Bolotin, K. J. Sikes, Z. Jiang, M. Klima, G. Fudenberg, J. Hone, P. Kim, and H. L. Stormer, "Ultrahigh electron mobility in suspended graphene," Solid State Commun. **146**(9-10), 351–355 (2008).
24. M. Poljak, T. Suligoj, and K. L. Wang, "Influence of substrate type and quality on carrier mobility in graphene nanoribbons," J. Appl. Phys. **114**(5), 053701 (2013).

Optics EXPRESS

25. A. Pirkle, J. Chan, A. Venugopal, D. Hinojos, C. W. Magnuson, S. McDonnell, L. Colombo, R. S. Vogel, R. S. Ruoff, and R. M. Wallace, "The effect of chemical residues on the physical and electrical properties of chemical vapor deposited graphene transferred to SiO_2," Appl. Phys. Lett. **99**(12), 122108 (2011).
26. J. Chan, A. Venugopal, A. Pirkle, S. McDonnell, D. Hinojos, C. W. Magnuson, R. S. Ruoff, L. Colombo, R. M. Wallace, and E. M. Vogel, "Reducing extrinsic performance-limiting factors in graphene grown by chemical vapor deposition," ACS Nano **6**(4), 3224–3229 (2012).
27. Y. Yao, R. Shankar, M. A. Kats, Y. Song, J. Kong, M. Loncar, and F. Capasso, "Electrically tunable metasurface perfect absorbers for ultrathin mid-infrared optical modulators," Nano Lett. **14**(11), 6526–6532 (2014).
28. J. R. Piper and S. Fan, "Total absorption in a graphene monolayer in the optical regime by critical coupling with a photonic crystal guided resonance," ACS Photonics **1**(4), 347–353 (2014).
29. G.-D. Liu, X. Zhai, H.-Y. Meng, Q. Lin, Y. Huang, C.-J. Zhao, and L.-L. Wang, "Dirac semimetals based tunable narrowband absorber at terahertz frequencies," Opt. Express **26**(9), 11471–11480 (2018).
30. X. Chen, Z. Tian, Y. Lu, Y. Xu, X. Zhang, C. Ouyang, J. Gu, J. Han, and W. Zhang, "Electrically tunable perfect terahertz absorber based on a graphene Salisbury screen hybrid metasurface," Adv. Opt. Mater. **8**(3), 1900660 (2020).
31. R. Alaee, M. Farhat, C. Rockstuhl, and F. Lederer, "A perfect absorber made of a graphene micro-ribbon metamaterial," Opt. Express **20**(27), 28017–28024 (2012).
32. J. Wu, "Ultra-narrow perfect graphene absorber based on critical coupling," Opt. Commun. **435**, 25–29 (2019).
33. X. Chen and W. Fan, "Tunable Bound States in the Continuum in All-Dielectric Terahertz Metasurfaces," Nanomaterials **10**(4), 623 (2020).
34. P. Q. Liu, I. J. Luxmoore, S. A. Mikhailov, N. A. Savostianova, F. Valmorra, J. Faist, and G. R. Nash, "Highly tunable hybrid metamaterials employing split-ring resonators strongly coupled to graphene surface plasmons," Nat. Commun. **6**(1), 8969 (2015).
35. S. Fan, W. Suh, and J. D. Joannopoulos, "Temporal coupled-mode theory for the Fano resonance in optical resonators," J. Opt. Soc. Am. A **20**(3), 569–572 (2003).
36. M. Grande, M. A. Vincenti, T. Stomeo, G. V. Bianco, D. de Ceglia, N. Aközbek, V. Petruzzelli, G. Bruno, M. De Vittorio, M. Scalora, and A. D'Orazio, "Graphene-based absorber exploiting guided mode resonances in one-dimensional gratings," Opt. Express **22**(25), 31511–31519 (2014).
37. Y. Long, L. Shen, H. Xu, H. Deng, and Y. Li, "Achieving ultranarrow graphene perfect absorbers by exciting guided-mode resonance of one-dimensional photonic crystals," Sci. Rep. **6**(1), 32312 (2016).
38. K. Ito and H. Iizuka, "Directional thermal emission control by coupling between guided mode resonances and tunable plasmons in multilayered graphene," J. Appl. Phys. **120**(16), 163105 (2016).
39. C.-C. Guo, Z.-H. Zhu, X.-D. Yuan, W.-M. Ye, K. Liu, J.-F. Zhang, W. Xu, and S.-Q. Qin, "Experimental demonstration of total absorption over 99% in the near infrared for monolayer-graphene-based subwavelength structures," Adv. Opt. Mater. **4**(12), 1955–1960 (2016).
40. B. Zhao and Z. M. Zhang, "Strong Plasmonic Coupling between Graphene Ribbon Array and Metal Gratings," ACS Photonics **2**(11), 1611–1618 (2015).
41. Y.-L. Liao and Y. Zhao, "Graphene-based tunable ultra-narrowband mid-infrared TE-polarization absorber," Opt. Express **25**(25), 32080–32089 (2017).
42. S. Cao, D. Zhang, and Q. Wang, "Graphene-based dynamically tunable absorbers through guided mode resonance," Superlattices Microstruct. **144**, 106550 (2020).
43. Y. Zhao, Y.-L. Liao, P. Wang, Y. Liu, Y. Gong, and W. Sheng, "Tunable ultra-narrowband mid-infrared absorber with graphene and dielectric metamaterials," Results Phys. **23**, 104038 (2021).
44. S. Lee, J. Song, and S. Kim, "Graphene perfect absorber with loss adaptive Q-factor control function enabled by quasi-bound states in the continuum," Sci. Rep. **11**(1), 22819 (2021).
45. X. Jiang, W. Liu, B. Zhang, and X. Sun, "Tunable ultra-high Q-factor and Figure of Merit based on Fano resonance in graphene-dielectric multilayer corrugated structure," Adv. Opt. Mater. **8**(24), 2001443 (2020).
46. L. A. Falkovsky, "Optical properties of graphene," J. Phys.: Conf. Ser. **129**, 012004 (2008).
47. Y. Yang and R. Murali, "Impact on size effect on graphene nanoribbon transport," IEEE Electron Device Lett. **31**(3), 237–239 (2010).
48. Y. Ding and R. Magnusson, "Doubly resonant single-layer bandpass optical filters," Opt. Lett. **29**(10), 1135–1137 (2004).
49. K. X. Wang, Z. Yu, S. Sandhu, and S. Fan, "Fundamental bounds on decay rates in asymmetric single-mode optical resonators," Opt. Lett. **38**(2), 100–102 (2013).